Matrix-Independent Surface-Enhanced Raman Scattering Detection of Uranyl Using Electrospun Amidoximated Polyacrylonitrile Mats and Gold Nanostars

Grace Lu[†,§], **Adam J. Johns**[†,‡], **Binita Neupane**[†], **Hoa T. Phan**[†], **David M. Cwiertny**[‡], **Tori Z. Forbes**[†,‡], and **Amanda J. Haes**[*,†]

[†]Department of Chemistry and Environmental Engineering, University of Iowa, Iowa City, Iowa 52242, United States

[‡]Department of Civil and Environmental Engineering, University of Iowa, Iowa City, Iowa 52242, United States

Abstract

Reproducible detection of uranyl, an important biological and environmental contaminant, from complex matrixes by surface-enhanced Raman scattering (SERS) is successfully achieved using amidoximated-polyacrylonitrile (AO-PAN) mats and carboxylated gold (Au) nanostars. SERS detection of small molecules from a sample mixture is traditionally limited by nonspecific adsorption of nontarget species to the metal nanostructures and subsequent variations in both the vibrational frequencies and intensities. Herein, this challenge is overcome using AO-PAN mats to extract uranyl from matrixes ranging in complexity including HEPES buffer, $Ca(NO_3)_2$ and $NaHCO_3$ solutions, and synthetic urine. Subsequently, Au nanostars functionalized with carboxyl-terminated alkanethiols are used to enhance the uranyl signal. The detected SERS signals scale with uranyl uptake as confirmed using liquid scintillation counting. SERS vibrational frequencies of uranyl on both hydrated and lyophilized polymer mats are largely independent of sample matrix, indicating less complexity in the uranyl species bound to the surface of the mats vs in solution. These results suggest that matrix effects, which commonly limit the use of SERS for complex sample analysis, are minimized for uranyl detection. The presented synergistic approach for isolating uranyl from complex sample matrixes and enhancing the signal using SERS is promising for real-world sample detection and eliminates the need of radioactive tracers and extensive sample pretreatment steps.

[*]Corresponding Author Phone: (319) 384-3695. amanda-haes@uiowa.edu.
[§]**Present Address**G.L.: C. Eugene Bennett Department of Chemistry, West Virginia University, Morgantown, WV 26506.

Author Contributions

All authors have given approval to the final version of the manuscript.

The authors declare no competing financial interest.

ASSOCIATED CONTENT

Supporting Information

The Supporting Information is available free of charge on the ACS Publications website at DOI:10.1021/acs.anal-chem.8b00655.

Synthesis, functionalization, and FT-IR characterization of electrospun PAN mats; additional details for U uptake on the mats; initial characterization of U uptake using LSC and Raman microscopy; synthesis, functionalization, and characterization of gold nanostars; detailed protocols for Raman and SERS data analysis; and summary of thermodynamic constants for uranyl speciation descriptions (PDF)

Graphical Abstract
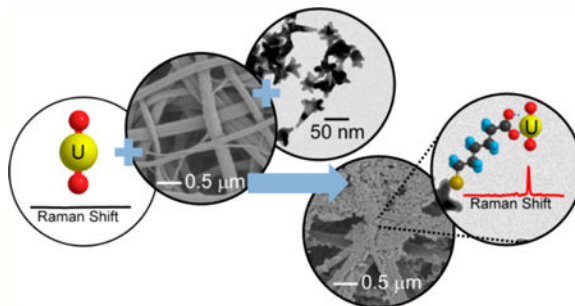
Hexavalent uranium (U), found in contaminated soils and water as the uranyl cation (UO_2^{2+}), presents a significant biological, chemical, and radiological threat[1,2] as chronic exposure promotes adverse health effects in at-risk populations. Uranium is a naturally occurring, radioactive element that decays by alpha emission ($t_{1,2} = 4.5 \times 10^9$ years) and is a widespread contaminant in the southwest United States where U concentrations in unregulated water sources can routinely exceed the U.S. EPA maximum contaminant level (30 μg/L U) by as much as 5-fold.[1,2] From a public health perspective, this chronic environmental exposure to U is concerning because it is a documented nephrotoxin, negatively impacts DNA repair, disrupts regulation of transcription factors and gene expression, and promotes apoptosis thus increasing the risk of cancer and other health problems.

Uranium detection in environmental and biological samples is the first step toward addressing public health concerns and environmental remediation of impacted lands, but there are issues with the complex nature of the matrix. In general, uranyl speciation in a biological or environmental sample is dynamic and complex and depends on the abundance of other ions, organic ligands, solid surfaces, and pH.[3–6] This complexity leads to problems in separations and data analysis; thus, samples are often altered using concentrated acids or separated using multistep, time intensive columns, and precipitation reactions.[7–10] After these pretreatment steps, traditional radiometric and analytical detection methods, such as alpha spectroscopy and mass spectrometry, provide excellent detection limits to quantify solution species but require expensive equipment and trained personnel. Thus, new approaches for simple and rapid detection of U from complex matrixes are needed.

Raman spectroscopy is an attractive alternative method for U detection because the symmetric stretch associated with the uranyl bond is readily detectable from 870 to 800 cm^{-1}. Furthermore, the vibrational frequencies of this bond are sensitive to inner sphere ligand coordination, providing additional speciation information, and spectral signal can be acquired in minutes.[11–15] Normal Raman spectroscopy, however, is limited by the inherently small Raman cross sections associated with molecules so must be used in conjunction with enhancement methods to achieve detectable signals. For instance, normal Raman signals can be enhanced by 2–9 orders of magnitude[16–18] using surface-enhanced Raman scattering (SERS).

SERS detection of uranyl is feasible[19–24] but limited by the inherent nonspecific adsorption of other molecules on SERS-active substrates[25] as well as the previously discussed complex and dynamic speciation of uranyl present in a complex sample matrix.[19–23] For instance, humic acid was shown to coordinate with uranyl affecting its speciation in solution, which in turn reduced the adsorption of uranyl to silver SERS substrates. This resulted in lower detectability of uranyl using SERS.[24]

In the current study, we demonstrate the development of a SERS-based method for the detection of U in buffer and in the presence of environmentally relevant confounding ions or synthetic urine by utilizing electrospun, amidoximated (AO) polyacrylonitrile (PAN) mats to extract U from solution and Au nanostars to enhance spectral signals (Figure 1). The key advancement of this approach is the use of AO-PAN mats to initially isolate and preconcentrate U from complex matrixes followed by SERS detection directly on the polymer mats. By doing so, Raman spectra become simplified and matrix effects minimized thereby providing fast, reproducible, and quantitative detection of uranyl from complex matrixes.

MATERIALS AND METHODS

Fabrication, Functionalization, and Characterization of Electrospun PAN Mats.

Detailed descriptions[26–29] of the fabrication and functionalized of the electrospun mats are found in the Supporting Information. Briefly, polymer mats are prepared stepwise by first spinning a polyvinylidene fluoride (PVDF) support layer onto a grounded drum collector. The PAN layer is subsequently electrospun on top of the PVDF. Once removed from the drum, nitrile groups in the polymeric mats are converted into amidoxime groups using reduction by hydroxylamine.[30,31] After functionalization, the mats are rinsed with DI water until the pH of the rinsewater is less than 7, placed on parafilm (PAN side up), dried for at least 12 h in air at room temperature, and stored at room temperature until use.

Scanning electron microscopy (SEM) is used to characterize the morphology and average fiber diameter of the polymer mats. Electrospun fibers are sputter coated with Au/Pd (Emitech Sputter Coater K550) then imaged using a Hitachi S-4800 SEM. Fiber diameter is analyzed using Image Pro. At least 100 measurements are used.

Uranyl Uptake and Validation.

Uranyl sorption is evaluated using 1 μM-10 mM U solutions by adding known amounts of a 1000 mg/L depleted uranium (SPEX CertiPrep) stock solution and 85.0 μL of ^{232}U radiotracer (LSC measurements only; 3.5 Bq, NIST traceable standard, Eckert & Ziegler) in 10 mM HEPES (pH 6.8; adjusted using 5 N NaOH or HCl), 3.4 mM $CaCl_2$, 5 mM $NaCO_3$, or 20 mL of Surine Negative Urine Control (Cerilliant). These solutions were chosen to reflect cosolutes and concentrations typical of U-containing groundwater samples. In total, 5 mg of the amidoximated composite mat (dry weight) is added to these solutions and incubated for 18 h. Each experiment is performed in triplicate with appropriate controls. Uranyl uptake is confirmed using liquid scintillation counting (LSC) and normal Raman microscopy (see the Supporting Information).

SERS Measurements and Analysis.

SERS measurements are collected using 6-mercaptohexanoic acid (6-MHA) functionalized Au nanostars. Previously reported protocols are used to generate these materials,[32] which are described in detail in the Supporting Information. The functionalized Au nano-stars are stored at concentrations of 0.3 nM in 5 mM EPPS until use. Immediately prior to use, the materials are concentrated to 8 nM using centrifugation ($2000g$; 40 min) and dispersed in an 80% ethanolic solution.

Nanostar structure is evaluated using transmission electron microscopy (TEM). A JEOL JEM-1230 TEM equipped with a Gatan CCD camera and a 120 keV acceleration voltage are used. Small volumes (10 μL) of the nanostars dispersed in 50% ethanol are deposited on 400 mesh copper grids coated with Formvar and carbon (Ted Pella). At least 100 Au nanostars are analyzed using Image Pro to evaluate the radius of curvature of the nanostar tips and the overall average sizes.

SERS measurements are collected using the same microscope setup used for normal Raman measurements. AO-PAN mats are diced into 3 mm × 3 mm squares. Next, 1 μL of the ethanolic Au nanostar solution is added every ~2 min until 10 μL of the solution is deposited on the mats, which are then allowed to equilibrate for 10 min. Mats evaluated in a hydrated state are placed on a microscope slide (PVDF side down) and covered by 50 μL of water. A coverslip is carefully placed over the hydrated mats so that no air bubbles are visible. Alternatively, mats are placed on a microscope slide (PVDF side down) and placed in a lyophilizer for 24 h prior to analysis. All measurements are collected using 785 nm excitation and at ambient conditions (20 °C and 30–40% relative humidity). Hydrated samples are collected using a 10× objective, power = 25 mW, and t_{int} = 30 s. Lyophilized samples are collected using a 20× objective, power = 1.5 mW, and t_{int} = 50 s. Five measurements from different locations are averaged. Reported spectra are raw minus identically collected spectra from a control (matrix only). Detailed spectral analysis was reported previously[13] and can be found in the Supporting Information.

RESULTS AND DISCUSSION

Characterization of and Uranyl Uptake on PAN and AO-PAN Mats.

Previous studies indicated that amidoximation[33–43] of PAN led to uranyl uptake that was dependent on pH, and additional gains in U extraction efficiency were achieved using high surface area to volume nanomaterials[44,45] and electrospun fibers.[43,46,47] Here, high surface area materials (surface area = 16.3 ± 0.6 m^2/g) used are integrated for Raman analysis in a stepwise fashion to maximize uranyl uptake and for reproducible and robust spectroscopic detection. As shown in Figure 1A, electrospun PAN fibers form a mat structure with an average fiber diameter (d) of 100 ± 30 nm. PAN mats are hydrophilic[48] but did not readily coordinate to uranyl (vide infra). Amidoximation of the PAN fibers (Figure 2A) does not significantly alter the average d (Figure 1B) of 110 ± 20 nm. FT-IR analysis confirms the presence of amidoxime groups on PAN after functionalization (see the Supporting Information), and spectra are similar to previous literature reports.[30,31]

Fiber diameters remain constant upon incubation with uranyl (Figure 1C, $d = 120 \pm 20$ nm). As shown in the photographs in Figure 1, successful uranyl uptake is confirmed visually by a slight yellowing of the AO-PAN mats when 10 μM uranyl concentrations are used. Time-dependent uranyl uptake data from HEPES buffer (pH 6.8) are summarized in Figure 2B. As incubation time increases, the amount of sorbed uranyl increases systematically during the first ~16 h before reaching sorption equilibrium. As a result, an 18 h incubation period is used for all subsequent uptake studies.

Additional sorption experiments with 1, 5, and 10 μM uranyl in the presence of 500 mg/L Ca^{2+} or 500 mg/L HCO_3^- as well as synthetic urine explore the influence of solution composition on uranyl uptake. Uptake in relatively idealized 10 mM HEPES is provided for comparison. As shown in Figure 2C, solution complexity produces no statistical difference in average uranyl uptake across the concentration range investigated for Ca^{2+} and HCO_3^-. Thus, uranyl binding by amidoxime groups on the AO-PAN surface appears relatively insensitive to environmental variables [e.g., components of hardness (Ca^{2+}) and alkalinity (HCO_3^-)] that often limit the capacity and selectivity of sorbents. Although uptake in synthetic urine is comparable to other matrixes when uranyl concentration is below 5 μM, uptake is significantly impacted by the matrix at the highest U concentration investigated. We attribute these uptake differences to variations in uranyl speciation in solution and/or the formation of insoluble U,[49] which reduces the effective concentration in solution.

Evaluation of Uranyl Uptake on AO-PAN Mats Using Normal Raman Spectroscopy.

Now that successful uranyl uptake for various sample matrixes has been confirmed, normal Raman detection is employed directly on lyophilized electro-spun AO-PAN mats using Raman microscopy through evaluation of the symmetric uranyl stretch. Near-infrared excitation and a 50× objective are used to minimize mat damage by the laser and to reduce implications of mat roughness on measurements, respectively. Uranyl coordinated to AO-PAN mats is confirmed in Figure 3A from the broad (full width at half-maximum, Γ, 46 and 57 cm^{-1} for pH 4 and 6.8, respectively) spectral feature centered at 818 cm^{-1}. Several important details are noted. First, the vibrational feature bandwidth is larger than that of a single solution-phase[13] uranyl species (~14–20 cm^{-1}). This suggests that the vibrational bands arise from uranyl coordinated to the AO-PAN mats (i.e., surface Raman spectra)[50] rather than from uranyl in solution. It is also possible that an increase in line width arises from multiple uranyl coordination geometries to the AO-PAN mat, but both hypotheses suggest that the UO_2^{2+} cation is bound to the mat surface. Next, the vibrational band intensity is ~1.6 times more intense when uranyl uptake occurs at pH 6.8 vs 4. Finally, intensities and Γ increase but vibrational frequencies remain constant when the solution pH used during uptake increases from 4 to 6.8. Because pH impacts both uranyl speciation[13] and AO-PAN functional group protonation,[39,41] both would influence the resulting vibrational features.

Previously, several computational and well-controlled experimental studies were conducted to decipher the structure of amidoxime and uranyl complexes[35,40,42] and formation constants.[34,37,39,41,51] We build on this excellent foundation for understanding these spectral features and uranyl binding mechanisms. First, we consider the pK_a values (assumed at

infinite dilution) of acetamidoxime (5.78 and 13.50)[39,41] as a model compound to gain insights on the thermodynamics of uranyl uptake on the functionalized mat surface.[39,41] These details are summarized in Figure 1A and Table S1. These pK_a data are based on experiments performed in solution (different from the AO-PAN surface chemistry, which is more complex and could slightly impact the thermodynamic parameters). In addition, the amidoximation process was previously shown to lead to carboxylate and cyclic amidoxime group formation, which further complicates uranyl speciation and uptake. Use of this simplified model, however, provides specific insights into U uptake mechanism and is corroborated by spectroscopy data as described in detail below.

At pH 4, the amidoxime groups are positively charged (protonated hydroxylamine or AOH_2^+), and uranyl uptake likely occurs via the formation of UO_2AO^+. In contrast, at pH 6.8 the amidoxime groups are mostly neutral (AOH) and/or deprotonated (AO^-) via residual hydroxide groups that remain on the hydrophilic polymer surface after functionalization. The resulting uranyl species would then be $UO_2AO(OH)$ and UO_2AO^+, respectively, as summarized in Scheme 1. Normal Raman spectra shown in Figure 3A support these coordination mechanisms. As mentioned previously, the uranyl line widths observed are consistent with surface-coordinated species. From the spectroscopic data and thermodynamic constants, we hypothesize that both $UO_2AO(OH)$ and UO_2AO^+ are isolated at pH 6.8 while only UO_2AO^+ forms at pH 4.

While the polymer mats are hydrophilic, hydration level influences swelling of the polymer mats,[52,53] which could induce slight vibrational frequency differences and irreproducibility in spectral intensities and band shapes. To improve measurement reproducibility, two approaches are used including evaluation of uranyl from AO-PAN mats in either hydrated or lyophilized states. First, AO-PAN mats are equilibrated in 1 and 10 mM uranyl then rinsed in water and buffer to remove weakly bound species. The mats are then immersed in buffer and evaluated using normal Raman microscopy. Representative spectra for 1 and 10 mM uranyl collected from hydrated mats are shown in Figure 3B–1, B-2, respectively. These spectra reveal that the vibrational bands associated with uranyl collected on hydrated mats are centered at 820 cm^{-1}, and band areas increase slightly as uranyl concentration increases. This signal is easily detectable above the noise likely because of uranyl preconcentration on the AO-PAN. As a comparison, normal Raman spectra of PAN and AO-PAN mats incubated in 1 mM uranyl is shown in Figure 4A–1, A-2, respectively. No uranyl signal is observed from the unfunctionalized mats. This is consistent with negligible uptake as quantified using LSC (0.37 ± 0.05 mg U per g mat). Uranyl uptake increases to 6.26 ± 1.33 mg U per g mat of AO-PAN and is confirmed from the small normal Raman signal observed in Figure 4A–2.

Similar trends are observed for AO-PAN mats incubated in uranyl then lyophilized. These data are summarized in Figure 3B–3, B-4 for 1 and 10 mM uranyl, respectively. First, similar increases in band area with increasing concentration are observed for the lyophilized vs hydrated mats. Two notable differences, however, are observed. First, the normal Raman vibrational frequency for uranyl is slightly blue-shifted from that observed on hydrated mats. The small 2 cm^{-1} blue-shift of the vibrational frequency to 818 cm^{-1} is attributed to solvation effects. Second, uranyl intensities are larger after lyophilization. Upon dehydration, the fibers deswell thus the amount of uranyl in the laser focal volume increases

thereby increasing the signal magnitude. As a result, concentration-dependent uranyl signals are reproducible if the hydration state of the mats is maintained during these vibrational spectroscopy measurements.

Maximizing and Understanding Uranyl Detection Using SERS and AO-PAN Mats.

Previously, we reported a SERS-based assay using solution-phase nanoparticles that resulted in the quantitative detection of uranyl down to 100 nM.[32] While reproducible measurements were achieved in buffer, uranyl detection was limited to solution conditions where nanoparticles retained their physical stability.[54] Using AO-PAN mats to extract uranyl from solution before SERS-active nanostructures are equilibrated with a sample is a plausible approach for achieving reproducible and enhanced detection of these chemical species. This is demonstrated in Figure 4A–3.

To attain this result, 6-MHA functionalized Au nanostars are added dropwise to AO-PAN mats after uranyl uptake and rinsing. TEM and SEM images of the Au nanostars and AO-PAN mats after nanostar deposition are shown in Figure 1E,D, respectively. The Au nanostars contain 3–7 spikes and average dimensions (diameter = 59.8 ± 14.0 nm, radius of curvature of tips = 3.8 ± 0.6 nm) consistent with previous reports.[32] When uranyl is present, the Au nanostars adhere to the fiber surfaces (Figure 1E). This observation is consistent with nanostar coordination via terminal carboxylate groups on the nanostars to uranyl bound to the AO-PAN mats.

To evaluate the impact of Au nanostar functionalization on uranyl detectability, SERS microscopy is used. As shown in Figure 4A–3, 10 μM uranyl is easily detected on hydrated AO-PAN mats. The vibrational frequency of uranyl is centered at 837 cm^{-1}, a value that is blue-shifted 17 cm^{-1} from the normal Raman mode. Because vibrational frequencies observed in SERS spectra typically red-shift relative to normal Raman frequencies (i.e., because bond lengths tend to increase upon interaction with nanomaterial surfaces),[20,23,55] we hypothesize that the carboxylate groups on the Au nanostars coordinate to uranyl upon disruption of uranyl coordination to AO groups on the mats as shown in Scheme 1C. This is further confirmed in that SERS enhancement of uranyl is not observed when unfunctionalized nanostars are used.

Uranyl coordination, however, likely depends on the density of both singly deprotonated amidoxime and 6-MHA groups on the Au nanostars. Because these values are not known quantitatively, we use SERS data to provide evidence in understanding how uranyl is coordinating to and/or interacting with the mats and nanostars for detection. To do this, SERS responses are collected from 10 μM uranyl incubated with 0.5 nM Au nanostars for 24 h at neutral pH. The solution is centrifuged for 5 min (2500g), the supernatant removed, and the loose pellet deposited on glass, PAN mats, and AO-PAN mats. SERS spectra of these samples are summarized in Figure 4B and vibrational mode frequency and lineshapes compared. These samples are selected because AO-PAN, PAN, and glass samples all contain carboxyl groups and amidoxime/nitrile, nitrile, and no other functional groups, respectively. Of note, only systematic and reproducible changes in uranyl vibrational modes are observed. Vibrational mode lineshapes are similar and vibrational frequencies are universally centered from 836 to 837 cm^{-1} (Γ = 30–35 cm^{-1}) in all spectra. This surprising result suggests that 6-

MHA on the Au nanostars disrupt uranyl coordination to the amidoxime groups because of high densities of 6-MHA molecules locally vs amidoxime as shown in Scheme 1.

Evaluating Matrix Effects in Uranyl Detection Using SERS.

To assess how matrix effects (a common limitation in SERS) impact SERS measurements, AO-PAN mats are incubated in 1–10 μM uranyl solutions adjusted to pH 6.8 in 10 mM HEPES with no other ion additions, 3.4 mM $Ca(NO_3)_2$, or 5 mM Na_2CO_3, or synthetic urine. This approach allows for the evaluation of how ideal solutions as well as those containing common confounding ions and U coordinating ligands at their relevant concentrations in groundwater (Ca^{2+} and CO_3^{2-}) and biological matrixes (synthetic urine) impact SERS detection.

Of note, SERS intensities directly correlate to the amount of U sorbed for each matrix and are summarized in Figure 5 and Table 1. Uranyl signals using both lyophilized (Figure 5A) and hydrated (Figure 5B) AO-PAN mats are shown. In general, uranyl successfully coordinates to AO-PAN mats and carboxylated Au nanostars in all conditions. This result is unexpected, and several trends are noted. First, on samples analyzed with SERS, LSC measurements confirm that slight signal variations arise from differences in U uptake. Second, differences in SERS spectral features in the uranyl window (i.e., vibrational frequency ($\bar{\nu}$), Γ, and/or integrated area of the entire uranyl window) are reproducible if mat areas with uniform nanoparticle deposition are sampled thus suggesting robust detection and largely sample matrix-independent SERS detection. This provides further evidence of the uranyl coordination mechanism proposed in Scheme 1. Of note, sample dryness is impacted by the relative humidity (30–40% RH) during data collection because of mat swelling. In addition, each spectrum collected using lyophilized mats contains a vibrational mode centered at 817 cm^{-1}. This band is attributed to a CH_2 bending mode from the 6-MHA molecules.[56] This band was previously observed for well-ordered, solid-like alkane monolayers. Because this band occurs in the uranyl window, it limits spectral interpretation and must be considered when quantifying uranyl signals on lyophilized mats. As such, SERS measurements using lyophilized AO-PAN mats must be done carefully so that reproducible uranyl detection is realized.

An alternative route for reproducible detection is to use hydrated AO-PAN mat samples. As shown in Figure 5B, samples collected from hydrated AO-PAN mats exhibit less intense uranyl vibrational modes; but these signals are more uniform, do not exhibit interference from the 6-MHA CH_2 bending mode, and reveal vibrational frequencies that are redshifted vs spectra collected using lyophilized samples. For example, SERS spectra collected from samples incubated in HEPES exhibit a uranyl band centered at 835 cm^{-1} (Figure 5B-1) when hydrated and 844 cm^{-1} (Figure 5A-1) upon lyophilization. A red-shifted vibrational frequency upon hydration is attributed to a reduction in Stark effects[57] as detailed in the Supporting Information and Table 1.

We hypothesize that hydration causes the polymers to swell by ~20% thus increasing the distance between nanostars on the polymer mats by ~15–20 times, which decreases the electric field strengths between the nanoparticles[58] (see the Supporting Information) in a sample matrix-dependent manner thus inducing a red-shift in each vibrational frequency

relative to the dehydrated samples. In addition to the vibrational frequency Stark effects, measurements collected on hydrated mats exhibit vibrational frequencies that differ by only ~2 cm^{-1} for all sample matrixes. The vibrational frequencies of uranyl in HEPES, Ca^{2+}, CO$_3^{2-}$, and synthetic urine are 835.3 ± 0.4, 832.8 ± 0.3, 835.0 ± 0.5, and 833.0 ± 0.6 cm^{-1}, respectively. Total integrated areas follow similar trends in the amount of U sorbed to the mats. That is, the largest signals are associated with samples incubated in HEPES followed by Ca^{2+} and CO$_3^{2-}$, then urine. While these trends can be partially attributed to different amounts of uranyl sorbed from the various sample matrixes, the SERS signals likely also depend on electro-magnetic coupling differences between Au nanostars on the AO-PAN mats.

Finally, evaluation of samples using both lyophilized and hydrated mats reveals useful information regarding uranyl coordination. For instance, all SERS spectra from lyophilized samples reveal intense (vs normal Raman and hydrated mat SERS measurements) vibrational bands with frequencies ranging from 845 to 844 cm^{-1} for samples incubated in HEPES and Ca^{2+} and ~845–830 cm^{-1} for carbonate and urine samples. This suggests that the ligands coordinated to uranyl are similar (in HEPES and Ca^{2+}) and distinct from the second two (CO$_3^{2-}$ and urine (PO$_4^{3-}$)). Furthermore, these bands are consistent with uranyl coordinated to a carboxylate group from 6-MHA on Au nanostars and possibly to hydroxide as proposed in Scheme 1. The vibrational frequencies observed for the carbonate and urine samples suggest that either carbonate or phosphate[59] (urine) is coordinated to uranyl. In addition, the signals collected from urine are relatively broad and contain multiple vibrational frequencies each of which could arise from uranyl species coordinating to phosphate and/or those interacting with cations (i.e., Na$^+$) or small organic molecules that are present in urine. Exact confirmation of the proposed U speciation is beyond the scope of this work and will be explored in future studies. Furthermore, the integrated areas in the uranyl vibrational window obtained from the SERS spectra from both lyophilized and hydrated mat samples follow trends consistent with variations in uranyl uptake (Figure 5C,D) obtained from LSC of uranyl uptake on the AO-PAN mats thus demonstrating the powerfulness of this approach for detecting uranyl in complex matrixes.

CONCLUSIONS

The successful sorption and detection of uranyl from four unique sample matrixes was achieved using AO-PAN mats followed by addition of 6-MHA functionalized Au nanostars and SERS. AO-PAN mats exhibit high surface areas that facilitate large scale fabrication and functionalization that are ideal for uranyl isolation from near-neutral pH solutions. This was verified using structural as well as spectroscopic characterization of the mats at each stage of fabrication and uranyl detection. By comparing vibrational band frequencies, a potential mechanism of uranyl uptake using AO-PAN mats and functionalized Au nanostars was proposed. This includes initial isolation of uranyl via amidoxime coordination to the equatorial plane of uranyl followed by replacement of these coordinating groups by locally high densities of carboxylate on the nanostars used for SERS detection. Given this likely coordination mechanism, simplified SERS spectra are observed from uranyl samples prepared in buffer, in the presence of confounding ions including Ca^{2+} and CO$_3^{2-}$, as well as synthetic urine. Vibrational frequencies collected using hydrated AO-PAN mats from all four

of these matrixes vary by only ~2 cm^{-1}. This result is impressive given large matrix effects are normally observed for uranyl detected from these solution conditions using traditional detection methodologies and with SERS in general. Thus, this study demonstrates that electrospun AO-PAN mats efficiently isolate uranyl from different matrixes and that the subsequent addition of functionalized Au nanostars results in simplified Raman features for reproducible and robust uranyl detection. This work lays the foundation for a promising method for the rapid detection of trace uranyl from complex sample matrixes that does not require radioactive tracers or sample pretreatment.

Supplementary Material

Refer to Web version on PubMed Central for supplementary material.

ACKNOWLEDGMENTS

REFERENCES

(1). Blake JM; Avasarala S; Artyushkova K; Ali A-MS; Brearley AJ; Shuey C; Robinson WP; Nez C; Bill S; Lewis J; Hirani C; Pacheco JSL; Cerrato JM Environ. Sci. Technol 2015, 49, 8506–8514. [PubMed: 26158204]

(2). U.S. Environmental Protection Agency. Pacific Southwest, Region 9, 2015.

(3). Bernhard G; Geipel G; Brendler V; Nitsche HJ Alloys Compd. 1998, 271–273, 201–205.

(4). Berto S; Crea F; Daniele PG; Gianguzza A; Pettignano A; Sammartano S Coord. Chem. Rev. 2012, 256, 63–81.

(5). Rout S; Ravi PM; Kumar A; Tripathi RM J. Radioanal. Nucl. Chem. 2015, 303, 2193–2203.

(6). Unsworth ER; Jones P; Hill SJ J. Environ. Monit. 2002, 4, 528–532. [PubMed: 12195995]

(7). Rosner G; Hoetzl H; Winkler R Fresenius' J. Anal. Chem. 1990, 338, 606–609.

(8). Martinez-Aguirre A; Garcia-Leon M Appl Radiat. Isot. 1996, 47, 1103–1108.

(9). Horwitz EP; Chiarizia R; Dietz ML; Diamond H; Nelson DM Anal. Chim. Acta 1993, 281, 361–372.

(10). Horwitz EP; Dietz ML; Chiarizia R; Diamond H; Maxwell SL, III; Nelson MR Anal. Chim. Acta 1995, 310, 63–78.

(11). Tsushima S Dalton Trans. 2011, 40, 6732–6737. [PubMed: 21611649]

(12). Nguyen Trung C; Begun GM; Palmer DA Inorg. Chem. 1992, 31 , 5280–5287.

(13). Lu G; Forbes TZ; Haes AJ Anal. Chem. 2016, 88, 773–780. [PubMed: 26607279]

(14). Foerstendorf H; Jordan N; Heim KJ Colloid Interface Sci. 2014, 416, 133–138.

(15). De Jong WA; Apra E; Windus TL; Nichols JA; Harrison RJ; Gutowski KE; Dixon DA J. Phys. Chem. A 2005, 109, 11568–11577. [PubMed: 16354049]

(16). Chu Y; Banaee MG; Crozier KB ACS Nano 2010, 4, 2804–2810. [PubMed: 20429521]

(17). Haynes CL; Van Duyne RP J. Phys. Chem. B 2003, 107, 7426–7433.

(18). Haynes CL; Yonzon CR; Zhang X; Van Duyne RP J. Raman Spectrosc. 2005, 36, 471–484.

(19). Teiten B; Burneau A J. Raman Spectrosc. 1997, 28, 879–884.

(20). Ruan C; Luo W; Wang W; Gu B Anal. Chim. Acta 2007, 605, 80–86. [PubMed: 18022414]

(21). Leverette CL; Villa-Aleman E; Jokela S; Zhang Z; Liu Y; Zhao Y; Smith SA Vib. Spectrosc. 2009, 50, 143–151.

(22). Dai S; Lee Y-H; Young JP Appl. Spectrosc. 1996, 50, 536–537.

(23). Bhandari D; Wells SM; Retterer ST; Sepaniak MJ Anal. Chem. 2009, 81, 8061–8067. [PubMed: 19737007]

(24). Bao L; Yan H; Mahurin SM; Gu B; Dai S ACS Symp. Ser. 2006, 943, 53–63.

(25). Taylor CE; Garvey SD; Pemberton JE Anal. Chem. 1996, 68, 2401–2408.

(26). Nalbandian MJ; Greenstein KE; Shuai D; Zhang M; Choa Y-H; Parkin GF; Myung NV; Cwiertny DM Environ. Sci. Technol. 2015, 49, 1654–1663. [PubMed: 25582552]

(27). Nalbandian MJ; Zhang M; Sanchez J; Choa Y-H; Cwiertny DM; Myung NV J. Mol. Catal A: Chem. 2015, 404–405, 18–26.

(28). Nalbandian MJ; Zhang M; Sanchez J; Choa Y-H; Nam J; Cwiertny DM; Myung NV Chemosphere 2016, 144, 975–981. [PubMed: 26433935]

(29). Nalbandian MJ; Zhang M; Sanchez J; Kim S; Choa Y-H; Cwiertny DM; Myung NV J. Hazard. Mater. 2015, 299, 141–148. [PubMed: 26101968]

(30). Horzum N; Munoz-Espi R; Glasser G; Demir MM; Landfester K; Crespy D ACS Appl. Mater. Interfaces 2012, 4, 6338–6345. [PubMed: 23092359]

(31). Horzum N; Ta çioglu D; Okur S; Demir MM Talanta 2011, 85, 1105–1111. [PubMed: 21726745]

(32). Lu G; Forbes TZ; Haes AJ Analyst 2016, 141, 5137–5143. [PubMed: 27326897]

(33). Li WP; Han XY; Wang XY; Wang YQ; Wang WX; Xu H; Tan TS; Wu WS; Zhang HX Chem. Eng. J. 2015, 279, 735–746.

(34). Leggett CJ; Endrizzi F; Rao L Ind. Eng. Chem. Res. 2016, 55, 4257–4263.

(35). Abney CW; Mayes RT; Piechowicz M; Lin Z; Bryantsev VS; Veith GM; Dai S; Lin W Energy Environ. Sci. 2016, 9, 448–453.

(36). Endrizzi F; Leggett CJ; Rao L Ind. Eng. Chem. Res. 2016, 55, 4249–4256.

(37). Endrizzi F; Melchior A; Tolazzi M; Rao L Dalton Trans. 2015, 44, 13835–13844. [PubMed: 25928044]

(38). Hirotsu T; Katoh S; Sugasaka K; Seno M; Itagaki T J. Chem. Soc., Dalton Trans. 1986, 1983–1986.

(39). Lashley MA; Mehio N; Nugent JW; Holguin E; Do-Thanh C-L; Bryantsev VS; Dai S; Hancock RD Polyhedron 2016, 109, 81–91.

(40). Mehio N; Ivanov AS; Williams NJ; Mayes RT; Bryantsev VS; Hancock RD; Dai S Dalton Trans. 2016, 45, 9051–9064. [PubMed: 26979403]

(41). Mehio N; Williamson B; Oyola Y; Mayes RT; Janke C; Brown S; Dai S Ind. Eng. Chem. Res. 2016, 55, 4217–4223.

(42). Tsantis ST; Zagoraiou E; Savvidou A; Raptopoulou CP; Psycharis V; Szyrwiel L; Holynska M; Perlepes SP Dalton Trans. 2016, 45, 9307–9319. [PubMed: 27184620]

(43). Horzum N; Shahwan T; Parlak O; Demir MM Chem. Eng. J. 2012, 213, 41–49.

(44). Sadeghi S; Azhdari H; Arabi H; Moghaddam AZ J. Hazard. Mater. 2012, 215–216, 208–216. [PubMed: 22947184]

(45). Zhuang Z; Chen H; Lin Z; Dang Z Environ. Sci.: Nano 2016, 3, 1254–1258.

(46). Lee HG; Sai-Anand G; Lee K-P; Kang S-W; Gopalan AI Sci. Adv. Mater. 2014, 6, 1365–1374.

(47). Zhang B; Guo X; Xie S; Liu X; Ling C; Ma H; Yu M; Li J RSC Adv. 2016, 6, 81995–82005.

(48). Tripathi BP; Dubey NC; Subair R; Choudhury S; Stamm M RSC Adv. 2016, 6, 4448–4457.

(49). Sutton M; Burastero SR Chem. Res. Toxicol. 2004, 17, 1468–1480. [PubMed: 15540945]

(50). Maya L Radiochim. Acta 1982, 31, 147–151.

(51). Tian G; Teat SJ; Zhang Z; Rao L Dalton Trans. 2012, 41, 11579–11586. [PubMed: 22801978]

(52). Buchanan KJ; Hird B; Letcher TM Polym. Bull. 1986, 15, 325–332.

(53). Stafie N; Stamatialis DF; Wessling M J. Membr. Sci. 2004, 228, 103–116.

(54). Wijenayaka LA; Ivanov MR; Cheatum CM; Haes AJ J. Phys. Chem. C 2015, 119, 10064–10075.

(55). Bao L; Mahurin SM; Haire RG; Dai S Anal. Chem. 2003, 75, 6614–6620. [PubMed: 16465717]

(56). Lucas LJ; Tellez C; Castilho ML; Lee CLD; Hupman MA; Vieira LS; Ferreira I; Raniero L; Hewitt KC J. Raman Spectrosc. 2015, 46, 434–446.

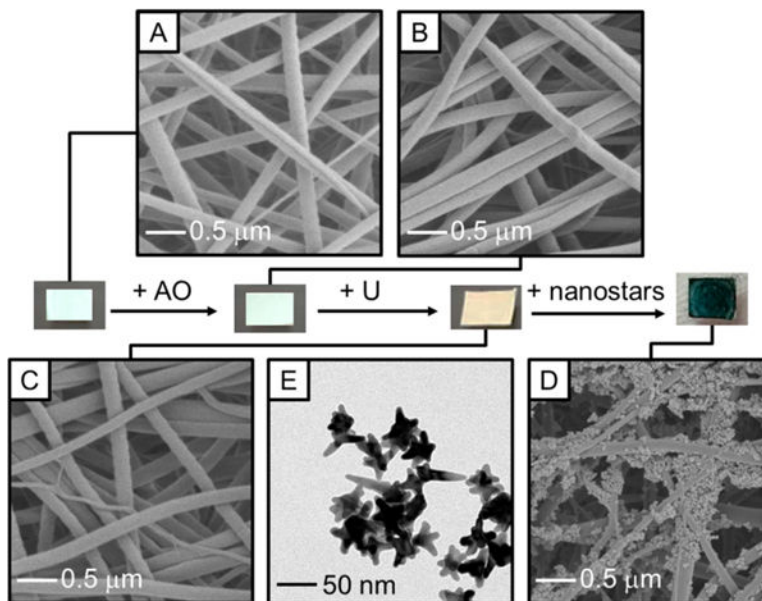(57). Kwasnieski DT; Wang H; Schultz ZD Chem. Sci. 2015, 6, 4484–4494. [PubMed: 26213606]

(58). Yang L; Li P; Liu H; Tang X; Liu J Chem. Soc. Rev. 2015, 44, 2837–2848. [PubMed: 25761511]

(59). Osman AAA; Geipel G; Barkleit A; Bernhard G Chem. Res. Toxicol. 2015, 28, 238–247. [PubMed: 25562669]

Figure 1.
Overview of the isolation and detection of uranyl using AO-PAN mats and Au nanostars. Representative photographs and SEM images of the PAN mats (A) as fabricated ($d = 101 \pm 28$ nm), after (B) AO functionalization ($d = 113 \pm 22$ nm), (C) uranyl uptake ($d = 116 \pm 24$ nm), and (D) Au nanostar deposition are shown. In addition, (E) TEM images of the 6-MHA functionalized Au nanostars are shown (size = 59.8 ± 14.0 nm).
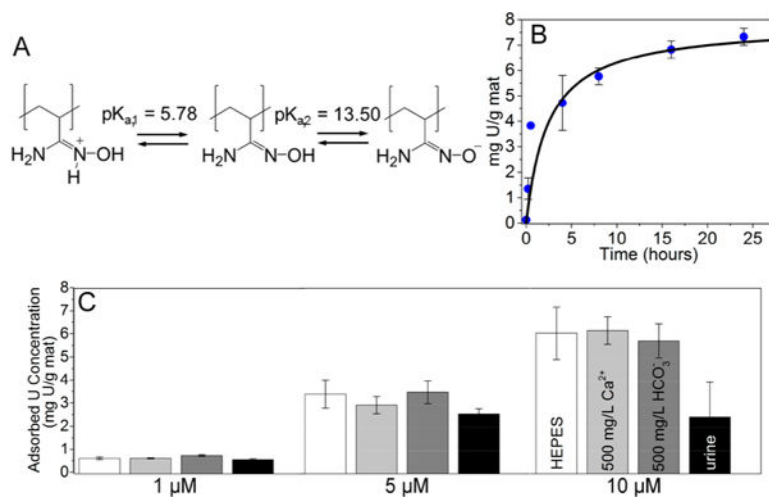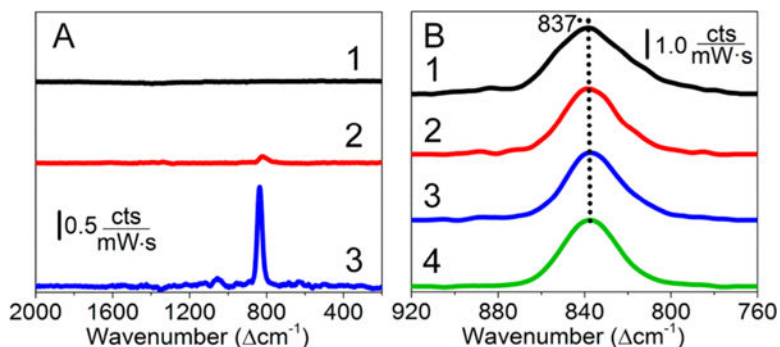
Figure 2.
Confirmation of U uptake. (A) Deprotonation of AO groups as a function of pH. (B) Evaluation of uranyl sorption as a function of incubation time using AO-PAN mats and LSC. A standard kinetic model is used to fit the data ($y = 8.5x/(4.43 + x)$). Error bars = standard deviations of 2+ measurements. (C) Adsorbed U determined using LSC as a function of initial U concentration in 10 mM HEPES buffer as well as in HEPES buffer with 500 mg/L of Ca^{2+} or HCO_3^- or synthetic urine.
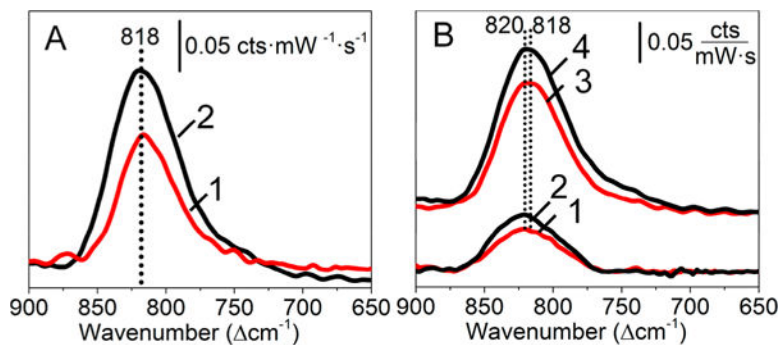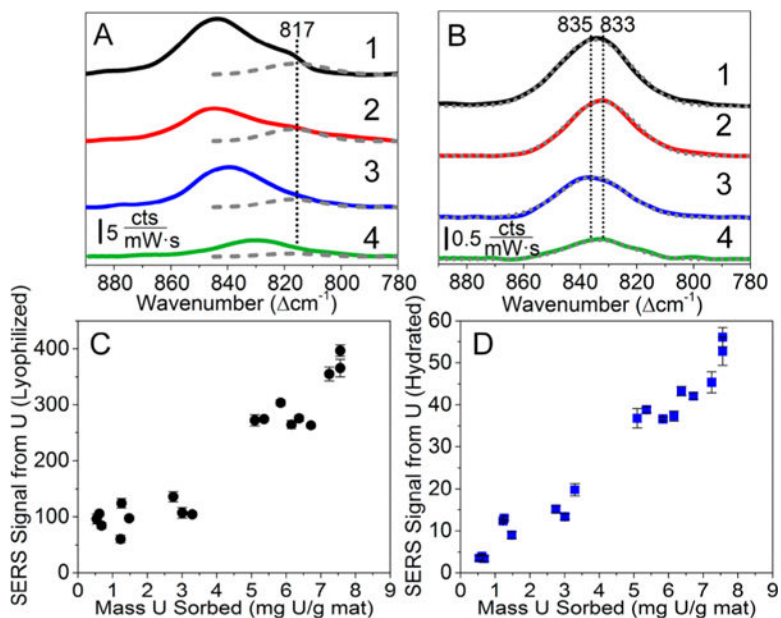
Figure 3.
Evaluation of uranyl detectability using Raman microscopy. (A) Normal Raman spectra of 10 mM uranyl uptake from pH (1) 4 and (2) 6.8 solutions onto lyophilized AO-PAN mats. (B) Normal Raman spectra of (1) 1 and (2) 10 mM uranyl collected using hydrated and (3) 1 and (4) 10 mM uranyl using lyophilized AO-PAN mats. Spectra are collected using the following parameters: λ_{ex} = 785 nm; t_{int} = 50 s, and P = 55 mW, 5 averages; 50× objective; 10 mM HEPES was used (18 h incubation).

Figure 4.
(A) Normal Raman spectra of 1 mM uranyl after uptake on hydrated (1) PAN and (2) AO-PAN mats as well as (3) a representative SERS spectrum of 10 μM uranyl after uptake on hydrated AO-PAN mats. (B) SERS spectra of 10 μM uranyl incubated with Au nanostars then deposited onto a (1) glass slide ($\bar{\nu} = 836.2 \pm 1.5\ cm^{-1}$ and $\Gamma = 35.2 \pm 1.5 cm^{-1}$), (2) PAN mat ($\bar{\nu} = 836.1 \pm 0.7\ cm^{-1}$ and $\Gamma = 30.9 \pm 1.0 cm^{-1}$), (3) AO-PAN mat ($\bar{\nu} = 837.1 \pm 0.5\ cm^{-1}$ and $\Gamma = 30.3 \pm 0.6 cm^{-1}$) and 10 μM uranyl (4) uptake on hydrated AO-PAN mats followed by addition of Au nanostars ($\bar{\nu} = 838.1 \pm 0.5\ cm^{-1}$ and $\Gamma = 30.3 \pm 1.0 cm^{-1}$). Collection conditions for normal Raman spectra are the same as in Figure 3. SERS collection parameters: $P = 25$ mW, $t_{int} = 30$ s, 10× objective (hydrated) or $P = 1.5$ mW, $t_{int} = 50$ s, 50× objective (lyophilized).

Figure 5.
SERS spectra of 10 μM uranyl (pH 6.8) in (1) 10 mM HEPES, (2) 3.4 mM Ca^{2+}, (3) 5 mM HCO_3^{2-}, and (4) synthetic urine using (A) lyophilized and (B) hydrated AO-PAN mats and 6-MHA functionalized Au nanostars. SERS on (C) lyophilized and (D) hydrated mats vs mass U sorbed determined by LSC. Error bars represent noise in each individual measurement. The CH_2 bending mode from 6-MHA is observed in lyophilized spectra and is centered at 817 cm^{-1}. All other spectral features are from uranyl (Table 1). Collection same as Figure 4.
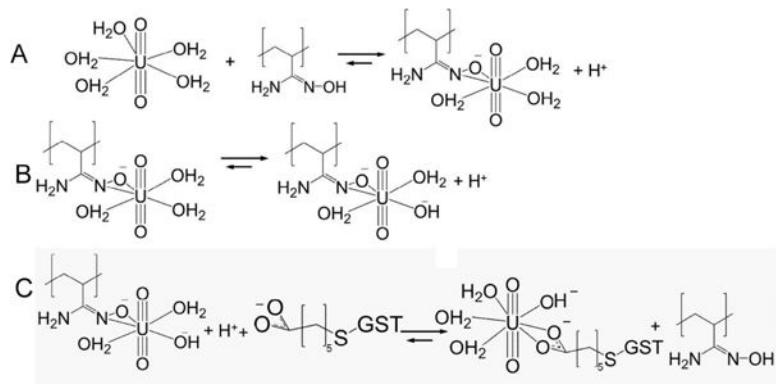
Scheme 1.
Proposed Pathway of Uranyl Uptake on AO-PAN Mats from Solution via Hydroxylamine Coordination to Uranyl with (A) All Aqua and (B) Two Aqua and One Hydroxyl Ligands and (C) Coordination with Carboxylic Acid from 6-MHA Functionalized Au Nanostars

Table 1.

Summary of U sorbed and correlated SERS Measurements in various sample matrixes

matrix	LSC mass U sorbed (mg U/g mat)	SERS (lyophilized) $\bar{\nu}$ (cm^{-1})	total integrated area (-MHA band)	SERS (hydrated) $\bar{\nu}$ (cm^{-1})	total integrated area	Γ (cm^{-1})	ratios of areas
HEPES	6.26 ± 1.33	844.4 ± 0.5	373 ± 22	835.3 ± 0.4	51.4 ± 5.4	31 ± 1	7.3
Ca^{2+}	5.99 ± 0.82	845.7 ± 0.4	267 ± 5	832.8 ± 0.3	38.7 ± 0.3	28 ± 1	6.9
HCO$_3^-$	5.73 ± 0.49	840.3 ± 1.1	284 ± 16	835.0 ± 0.5	39.6 ± 0.3	30 ± 2	7.2
s urine	2.48 ± 1.50	$831.9 \pm 1.1,$ 845.2 ± 3.0	79 ± 24	833.0 ± 0.6	11.4 ± 2.1	26 ± 1	6.9